*J. Fluid Mech.* (1998), *vol.* 366, *pp.* 311–331. Printed in the United Kingdom



# Transitions to complex flows in the Ekman–Couette layer

By N. HOFFMANN, F. H. BUSSE AND W.-L. CHEN

Institute of Physics, University of Bayreuth, D-95440 Bayreuth, Germany

(Received 9 July 1997 and in revised form 19 November 1997)

Secondary and tertiary states of fluid flow in a layer between two plates in relative motion and rotating about a normal axis of rotation are studied numerically for a wide range of parameters. Plane Couette flow without rotation and the single Ekman layer at a rigid plate above a quiescent fluid half-space are obtained as limiting cases. A Galerkin method is used for the investigation of the bifurcation structures of the problem. A Chebyshev collocation scheme is used for following the evolution of time-dependent states of the flow. Comparisons are made with experimental observations as well as with previous studies of particular parameter limits.

## 1. Introduction

As one of the few exact solutions of the Navier–Stokes equations, the Ekman layer represents the best known example of flows with varying direction. Its instabilities have been explored in the 1960s, but relatively little work has been devoted to the study of finite-amplitude secondary states of flow and higher bifurcations. In this paper the problem will be considered in the form of a sheared fluid layer which is rotating about an axis normal to the layer. Without the effects of rotation the problem corresponds to plane Couette flow as the basic solution. As the rate of rotation increases, the shear becomes increasingly confined to Ekman layers close to the rigid plates. The problem to be considered thus includes the plane Couette flow and the Ekman layer as limiting cases and therefore has been named the Ekman–Couette problem.

Laboratory experiments can only approximate the idealized configuration of the Ekman–Couette problem. A simple approximate realization is obtained when two circular parallel plates are rotated differentially about their common axis. A survey of the experimental results has been given by Zandbergen & Dijkstra (1987). Among the more recent experimental papers we mention Jarre, Le Gal & Chauve (1996) and Schouweiler *et al.* (1996). The spatial inhomogeneity of typical experiments with rotating disks allows only for local applications of the theory developed for the homogeneous case. Nevertheless, semiquantitative comparisons are possible as we shall point out at several places in this paper.

After a presentation in § 2 of the mathematical formulation of the problem and the numerical methods used for its solution we shall first discuss in § 3 the onset of Ekman layer instabilities in the present context. Their evolution to finite amplitude and their instabilities are described in §§ 4 and 5. In the following section the properties of tertiary solutions will be considered. In § 7 some unusual solutions and time-dependent phenomena will be mentioned. The paper closes in the concluding section with remarks on applications and on unresolved problems.

## 2. Mathematical formulation of the problem

We consider a fluid layer between two parallel plates which move with the velocity $U_D$ relative to each other in a system which is rotating about an axis normal to the plates with the angular velocity $\Omega_D$. We shall use the distance $h$ between the plates as length scale and $h^2/\nu$ as time scale where $\nu$ is the kinematic viscosity of the fluid. The Navier–Stokes equations of motion for the dimensionless velocity vector $\boldsymbol{v}$ assume the form

$$\frac{\partial}{\partial t}\boldsymbol{v} + \boldsymbol{v}\cdot\nabla\boldsymbol{v} + 2\Omega\boldsymbol{k}\times\boldsymbol{v} = -\nabla\pi + \nabla^2\boldsymbol{v}, \tag{2.1a}$$

$$\nabla\cdot\boldsymbol{v} = 0, \tag{2.1b}$$

where the unit vector $\boldsymbol{k}$ normal to the plates has been introduced. The boundary conditions can be written in the form

$$\boldsymbol{v} = \mp\boldsymbol{i}Re/2 \quad \text{at} \quad z = \pm\tfrac{1}{2} \tag{2.2}$$

where we have introduced a Cartesian system of coordinates with the $z$-coordinate in the direction of $\boldsymbol{k}$ and the $x$-coordinate in the direction of the unit vector $\boldsymbol{i}$ which describes the direction of the relative motion of the plates. The problem is characterized by two dimensionless parameters, the Reynolds number $Re$ and the rotation parameter $\Omega$ which are defined by

$$Re = \frac{U_D h}{\nu}, \quad \Omega = \frac{\Omega_D h^2}{\nu}. \tag{2.3}$$

The geometric configuration of the problem with the dimensionless parameters is shown in figure 1. We have chosen $\Omega$ as a parameter instead of the familiar Ekman number which corresponds to the inverse of $\Omega$. Since, in principle, contact can be made with the tertiary and quaternary solutions found in the plane Couette flow limit $\Omega = 0$ – for a discussion of recent results see Clever & Busse (1997) – $\Omega$ has been chosen as the most convenient rotation parameter. A basic steady solution of equations (2.1), (2.2) which reflects the homogeneity in the $x$- and $y$-dimensions of the problem can easily be obtained:

$$\boldsymbol{v} = \boldsymbol{U}_0 = (U_{0x}(z), U_{0y}(z), 0) \tag{2.4}$$

with

$$\begin{aligned} U_{0x} &= -A\sin(\Omega^{1/2}z)\cosh(\Omega^{1/2}z) + B\cos(\Omega^{1/2}z)\sinh(\Omega^{1/2}z), \\ U_{0y} &= +A\cos(\Omega^{1/2}z)\sinh(\Omega^{1/2}z) + B\sin(\Omega^{1/2}z)\cosh(\Omega^{1/2}z), \\ A[\sin(\Omega^{1/2}/2)\cosh(\Omega^{1/2}/2)]^{-1} &= -B[\cos(\Omega^{1/2}/2)\sinh(\Omega^{1/2}/2)]^{-1} \\ &= \frac{Re}{2}[\sin^2(\Omega^{1/2}/2)\cosh^2(\Omega^{1/2}/2) + \cos^2(\Omega^{1/2}/2)\sinh^2(\Omega^{1/2}/2)]^{-1}. \end{aligned}$$

In figure 2 the shear exerted by the flow (2.4) at the boundaries has been plotted. Since the shear is proportional to $Re$ we have used the normalized quantity

$$Sh = \left[\left(\frac{\partial}{\partial z}U_x\left(\tfrac{1}{2}\right)\right)^2 + \left(\frac{\partial}{\partial z}U_y\left(\tfrac{1}{2}\right)\right)^2\right]^{1/2} Re^{-1} \tag{2.5a}$$

which is independent of $Re$. From the value 1 at $\Omega = 0$, $Sh$ increases rapidly with increasing $\Omega$ to assume the $\Omega^{1/2}$-dependence characteristic of Ekman layers. Also

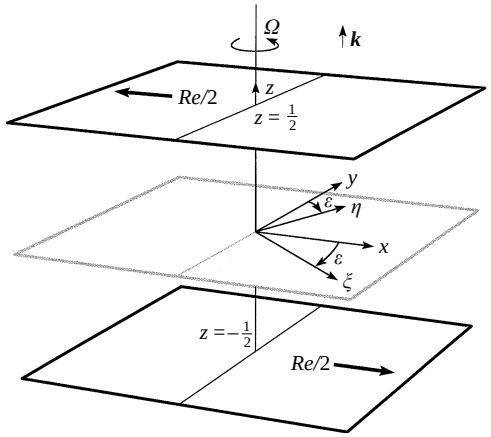


FIGURE 1. Geometrical configuration of the Ekman–Couette layer.

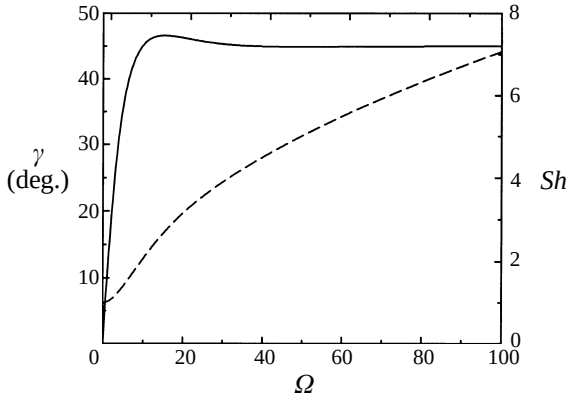


FIGURE 2. The angle $\gamma$ (solid lines, in degrees) between the direction of the shear at the boundaries and the $x$-axis. The normalized shear $Sh$ (dashed line) is measured by the right ordinate.

plotted is the angle $\gamma$ defined by

$$\gamma = \arctan\left(\left.\frac{\partial U_y}{\partial z}\right|_{z=1/2} \Big/ \left.\frac{\partial U_x}{\partial z}\right|_{z=1/2}\right) \tag{2.5b}$$

which measures the direction of the shear with respect to the $x$-axis. It is remarkable how quickly $\gamma$ attains its asymptotic value of 45° with increasing $\Omega$ in the case of solution (2.4). As can be seen from the figure, $\gamma$ even overshoots the asymptotic value for a small interval of $\Omega$.

The goal of the analysis of the paper is to identify and describe other solutions besides the basic solution of the problem. For this purpose we use the general representation for a solenoidal vector field $\boldsymbol{v}$:

$$\boldsymbol{v} = \boldsymbol{U} + \nabla \times (\nabla \times \boldsymbol{k}\phi) + \nabla \times \boldsymbol{k}\psi \equiv \boldsymbol{U} + \boldsymbol{\delta}\phi + \boldsymbol{\varepsilon}\psi = \boldsymbol{U} + \boldsymbol{u} \tag{2.6a}$$

where the scalar functions $\phi$ and $\psi$ can be chosen such that their $x, y$-average – indicated by a bar – vanishes:

$$\bar{\phi} = \bar{\psi} = 0, \quad \bar{\boldsymbol{v}} = \boldsymbol{U} \equiv \boldsymbol{U}_0 + \hat{\boldsymbol{U}}. \tag{2.6b, c}$$

The equations for $\phi, \psi$ are obtained in the form of the $z$-components of the (curl)$^2$ and of the curl of equation (2.1$a$),

$$\nabla^4\Delta_2\phi - 2\Omega\frac{\partial}{\partial z}\Delta_2\psi = \boldsymbol{k}\cdot\nabla\times(\nabla\times(\boldsymbol{u}\cdot\nabla\boldsymbol{u})) + \left(\frac{\partial}{\partial t} + \boldsymbol{U}\cdot\nabla\right)\nabla^2\Delta_2\phi - \frac{\partial^2}{\partial z^2}\boldsymbol{U}\cdot\nabla\Delta_2\phi, \quad (2.7a)$$

$$\nabla^2\Delta_2\psi + 2\Omega\frac{\partial}{\partial z}\Delta_2\phi = -\boldsymbol{k}\cdot\nabla\times(\boldsymbol{u}\cdot\nabla\boldsymbol{u}) + \left(\frac{\partial}{\partial t} + \boldsymbol{U}\cdot\nabla\right)\Delta_2\psi - \frac{\partial}{\partial z}\boldsymbol{U}\cdot\boldsymbol{\varepsilon}\Delta_2\phi, \quad (2.7b)$$

where the two-dimensional gradient operator, $\nabla_2 = (\partial/\partial x, \partial/\partial y, 0)$ and the two-dimensional Laplacian, $\Delta_2 = \nabla_2\cdot\nabla_2$, have been introduced. Equations (2.7$a, b$) offer the advantage that instead of four equations for the fluctuating components of the velocity field and of the dimensionless pressure $\pi$, only two equations for the scalar functions $\phi$ and $\psi$ must be considered. The equation for the deviation $\hat{\boldsymbol{U}}$ of the mean flow from the basic solution (2.4) is given by

$$\left(\frac{\partial^2}{\partial z^2} - \frac{\partial}{\partial t}\right)\hat{\boldsymbol{U}} + 2\Omega\boldsymbol{k}\times\hat{\boldsymbol{U}} = -\frac{\partial}{\partial z}\overline{\left(\Delta_2\phi\left(\frac{\partial}{\partial z}\nabla_2\phi + \boldsymbol{\varepsilon}\psi\right)\right)}. \quad (2.7c)$$

Equations (2.7) must be solved subject to boundary conditions

$$\phi = \frac{\partial}{\partial z}\phi = \psi = 0, \quad \hat{\boldsymbol{U}} = 0 \quad \text{at} \quad z = \pm\tfrac{1}{2}. \quad (2.8)$$

In order to obtain steady or time-dependent solutions in the form of two-dimensional rolls we use the Galerkin representation

$$\phi = \sum_{m,n} a_{mn}\exp\{\mathrm{i}ma\eta\}g_n(z), \quad (2.9a)$$

$$\psi = \sum_{m,n} b_{mn}\exp\{\mathrm{i}ma\eta\}\sin n\pi\left(z + \tfrac{1}{2}\right), \quad (2.9b)$$

$$\hat{\boldsymbol{U}} = \sum_{n} \boldsymbol{d}_n\sin n\pi\left(z + \tfrac{1}{2}\right), \quad (2.9c)$$

where the coefficients $a_{mn}, b_{mn}, \boldsymbol{d}_n = (d_{xn}, d_{yn}, 0)$ can be functions of time and where the coordinates $\xi, \eta$ are related to $x, y$ by the transformation

$$\begin{pmatrix} \xi \\ \eta \end{pmatrix} = \begin{pmatrix} \cos\varepsilon & -\sin\varepsilon \\ \sin\varepsilon & \cos\varepsilon \end{pmatrix}\begin{pmatrix} x \\ y \end{pmatrix} \quad (2.10)$$

as indicated in figure 1. Since the symbol $\varepsilon$ is used in the literature for the angle between the two coordinate systems we do not wish to introduce a new symbol. We expect that the scalar variable $\varepsilon$ will not be confused with the vector operator $\boldsymbol{\varepsilon}$ introduced in (2.6$a$). The latter symbol will not be needed anymore in the following. The $z$-dependence of the functions in the representation (2.9) is chosen such that the boundary conditions (2.8) are satisfied. In particular the functions

$$g_n(z) = \begin{cases} \dfrac{\cosh\lambda_n z}{\cosh\lambda_n/2} - \dfrac{\cos\lambda_n z}{\cos\lambda_n/2} & \text{for odd } n \\ \dfrac{\sinh\lambda_n z}{\sinh\lambda_n/2} - \dfrac{\sin\lambda_n z}{\sin\lambda_n/2} & \text{for even } n \end{cases} \quad (2.11a)$$

first introduced by Chandrasekhar (1961) are used where the $\lambda_n$ are determined as

roots of the equations

$$\tanh \lambda/2 + \tan \lambda/2 = 0 \text{ for odd } n, \quad \coth \lambda/2 - \cot \lambda/2 = 0 \text{ for even } n. \tag{2.11b}$$

In the case of a steady solution of the form (2.9) with constant coefficients $a_{mn}, b_{mn}, \boldsymbol{d}_n$, the stability can be investigated through the superposition of infinitesimal disturbances of the form

$$\tilde{\phi} = \exp\{\mathrm{i}d\xi + \mathrm{i}b\eta + \sigma t\} \sum_{m,n} \tilde{a}_{mn} \exp\{\mathrm{i}ma\eta\} g_n(z), \tag{2.12a}$$

$$\tilde{\psi} = \exp\{\mathrm{i}d\xi + \mathrm{i}b\eta + \sigma t\} \sum_{m,n} \tilde{b}_{mn} \exp\{\mathrm{i}ma\eta\} \sin n\pi \left(z + \tfrac{1}{2}\right), \tag{2.12b}$$

In contrast to the summations in expressions (2.9) which exclude the case $m = 0$ because of condition (2.6*b*), this case is included in the summations in (2.12) unless $d = b = 0$. Only in the latter case must a disturbance of the mean flow be considered. In practice, however, the limit $b = d = 0$ can be approached numerically without difficulty since the eigenvalues $\sigma$ depend smoothly on the Floquet wavenumbers $b, d$. The equations for the coefficients $a_{mn}, b_{mn}$ are obtained through projection of equations (2.7) onto the space of the expansion functions. Analogously the linear algebraic system of equations for the coefficients $\tilde{a}_{mn}, \tilde{b}_{mn}$ is obtained from the linearized versions of equations (2.7) for the disturbances. For a given steady solution characterized by the parameters $Re, \Omega, a$ and $\varepsilon$ the growth rates $\sigma$ must be determined as functions of $b$ and $d$. Whenever a positive real part $\sigma_r$ of $\sigma$ is found, the steady solution is unstable; otherwise it is regarded as stable.

For the numerical analysis the infinite number of coefficients and corresponding equations must be truncated. We shall use the 'diagonal' truncation rule in which all coefficients satisfying

$$m + n > N_T \tag{2.13}$$

are neglected. The truncation parameter $N_T$ must be chosen sufficiently large such that properties of physical interest do not change significantly when $N_T$ is replaced by $N_T - 2$. A typical value of $N_T$ used in the following analysis is $N_T = 10$, but values up to $N_T = 16$ have been used when necessary. For a more detailed discussion of the numerical method we refer to the paper by Clever & Busse (1997).

## 3. Instabilities of the basic Ekman–Couette state

For the study of the instability of the basic state there is no need to use the Galerkin approach since the usual shooting method based on a Runge–Kutta integration scheme for the linearized version of equations (2.7) is more economical from the computational point of view. The eigensolutions of the problem can be written in the form

$$\phi = \exp\{\mathrm{i}a\eta + \sigma t\} g(z), \tag{3.1a}$$

$$\psi = \exp\{\mathrm{i}a\eta + \sigma t\} f(z), \tag{3.1b}$$

where the functions $g(z), f(z)$ are to be determined by numerical integrations of ordinary differential equations; see, for example, Press *et al.* (1986). As the minimum Reynolds number $Re_c$ for growth rates $\sigma$ with real part $\sigma_r = 0$ is determined as function of $\Omega$ through variations of the parameters $\varepsilon$ and $a$, two distinct regimes are found. For low values of $\Omega$, i.e. $\Omega \lesssim 25$, the onset of instability occurs in the form of steady rolls with an axis of point symmetry on the midplane of the layer as

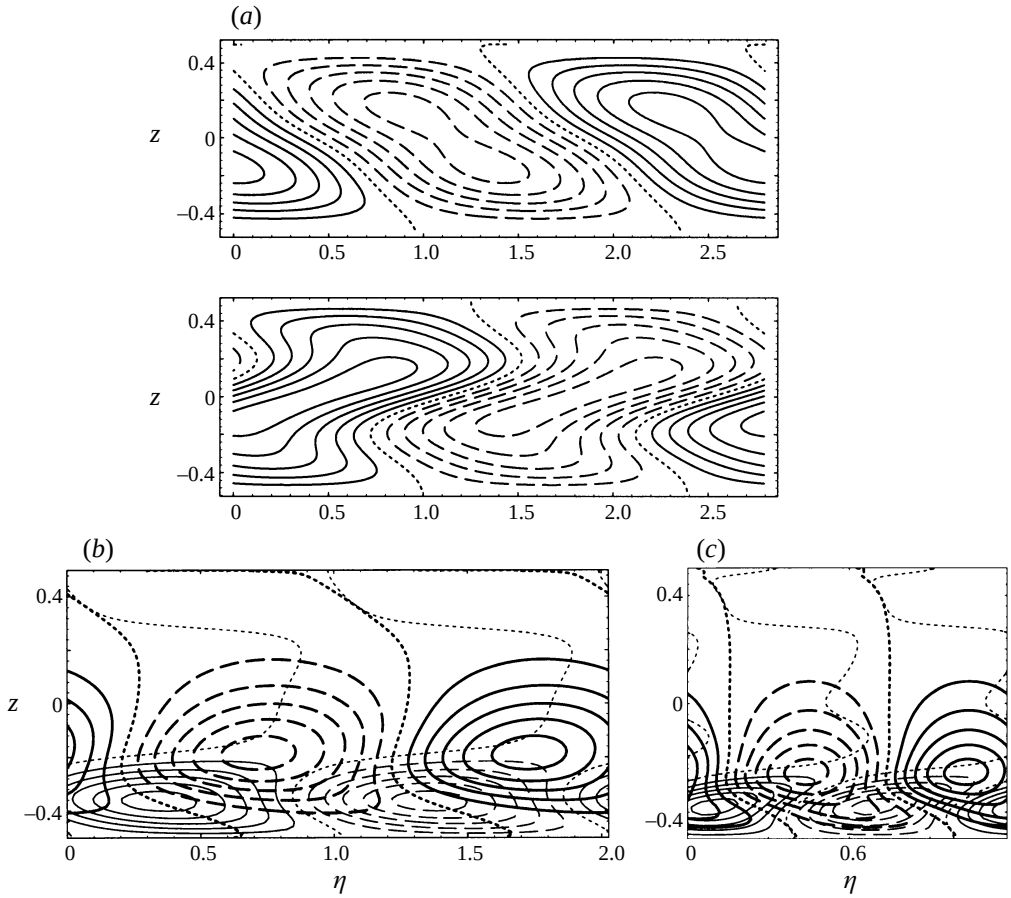


FIGURE 3. (*a*) Streamlines (upper plot) and lines of constant velocity in the $\xi$-direction (lower plot) for the steady roll mode of instability in the case $\Omega = 17$, $a = 2.55$, $\varepsilon = 8°$. Solid (dashed) lines indicate positive (negative) values. Dotted lines indicate zero. (*b*) Streamlines (thick lines) and lines of constant velocity in the $\xi$-direction (thin lines) for the type II instability in the case $\Omega = 100$, $Re = 1105$, $a = 3.3$, $\varepsilon = 23°$, $\sigma_i = 398$. (*c*) Same as (*b*) for the type I instability in the case $\Omega = 100$, $Re = 2245$, $a = 5.5$, $\varepsilon = -6.9°$, $\sigma_i = 1334$.

shown in figure 3(*a*). For large values of $\Omega$, i.e. $\Omega \gtrsim 25$, the Ekman nature of the instabilities predominates. Modes with finite imaginary part $\sigma_i$ become preferred. They are asymmetric with respect to the midplane of the layer and their time dependence mainly reflects the advection with one or the other Ekman layer near the rigid boundaries. As is well known from the single-Ekman-layer limit, $\Omega \to \infty$, there are two different types of these instabilities: type I characterized by a negative $\varepsilon$ and a relatively high wavenumber and type II with a positive $\varepsilon$ and a smaller wavenumber. These instabilities were first observed in the experiments of Faller (1962) and Tatro & Mollo-Christensen (1967). For theoretical investigations of these instabilities: see Faller & Kaylor (1966) and Lilly (1966). The form of secondary motions induced by these instabilities is visualized in figure 3(*b*, *c*) for the present case of finite $\Omega$.

A plot of the critical Reynolds numbers for the different mechanisms of instability is shown in figure 4. Also shown are the associated frequencies, wavenumbers $a$ and angles $\varepsilon$. The Reynolds numbers and the wavenumbers for the onset of the type I

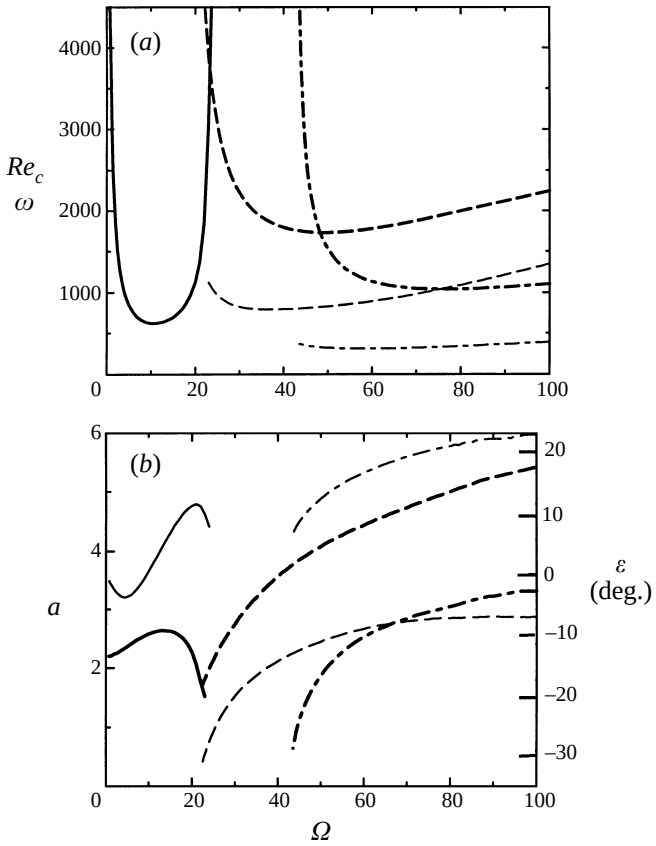


FIGURE 4. (*a*) Critical Reynolds numbers $Re_c$ (thick lines) for the onset of disturbances of the steady modes (solid line) and modes for type I (dashed) and type II (long dash–short dash lines). The frequencies $\omega = \sigma_i$ for the latter modes are indicated by thin lines. (*b*) The wavenumbers $a$ (thick lines) and angles $\varepsilon$ (thin lines) corresponding to the critical values $Re_c$ of (*a*).

and type II instabilities exhibit the expected square-root dependence on $\Omega$ for large $\Omega$ since the Ekman layer thickness decreases with $\Omega^{-1/2}$. The asymptotic limit of a single Ekman layer is also quantitatively well approached as can be judged by the comparison with the results of Lilly (1966) given in table 1. The relationship between the instabilities of type I and type II can be best visualized in the form of the neutral surface $\sigma_r = 0$ in the three-dimensional space spanned by the parameters $a, \varepsilon$ and $Re$ as shown in figure 5(*a*). The growth rates above the broad minimum of the Reynolds number for the onset of the type II Ekman layer instability remain relatively weak in comparison with those of type I and, for this reason, the former instability was overlooked in the original experiment of Faller (1962) and has been identified only in the later work of Tatro & Mollo-Christensen (1967).

Of particular interest in the present context of the Ekman–Couette problem is the intermediate region $20 \leqslant \Omega \leqslant 55$ which includes the codimension-two points at $\Omega = 24$ and at $\Omega = 48$ as indicated in figure 4(*a*). The topology of the neutral surface of figure 5(*a*) becomes distorted as $\Omega$ is decreased and a return to negative growth rates of the type II instability with increasing $Re$ can be noticed in the three-dimensional plot of figure 5(*b*). The evolution of instabilities in the neighbourhood of

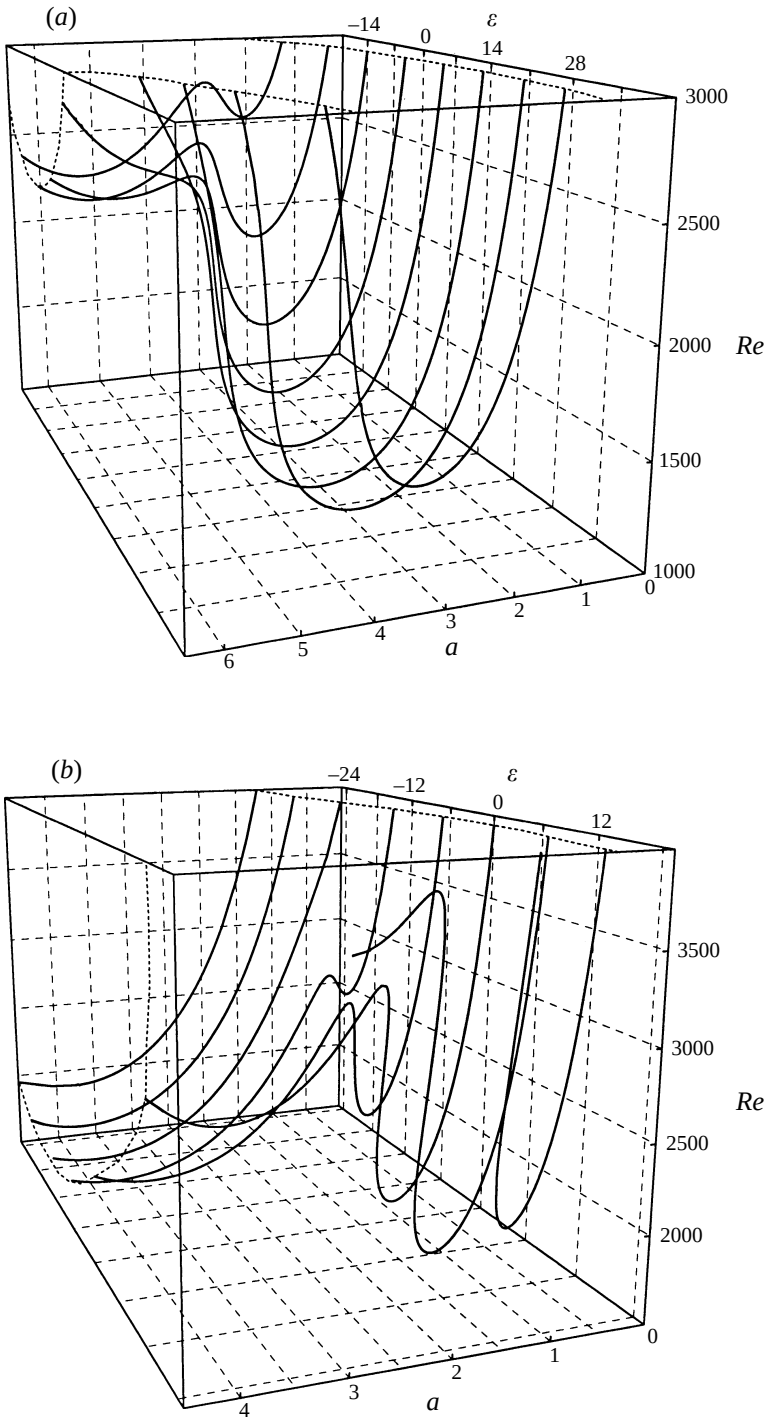


FIGURE 5. (*a*) The surface $\sigma_r = 0$ in the $Re, a, \varepsilon$ space for $\Omega = 100$. The local minimum of $Re$ corresponds to the onset of type I and type II instabilities, respectively. Same as (*b*), but for $\Omega = 48$.

| | | $Re_c$ | $a$ | $\varepsilon$ (deg.) | $\omega$ | $Re_{cL}$ | $a_L$ | $\varepsilon_L$ (deg.) | $c_L/c_{gL}$ |
|---|---|---|---|---|---|---|---|---|---|
| Results of this paper | Type I | 2244.6 | 5.5 | −6.88 | 1346.5 | 112.2 | 0.55 | 6.88 | 0.0984 |
| | Type II | 1105.3 | 3.3 | 22.9 | 391.2 | 55.3 | 0.33 | −22.9 | −0.6039 |
| Lilly's (1966) results | Type I | — | — | — | — | 112 | 0.55 | 6.8 | 0.104 |
| | Type II | — | — | — | — | 55 | 0.33 | −22.6 | −0.600 |

TABLE 1. Onset of instabilities of types I and II at $\Omega = 100$ and a comparison with the results of Lilly (1966) for a single Ekman layer. For the comparison the results have been transformed to quantities as used by Lilly which are indicated by the subscript $L$. $c, c_g$ denote the phase and group velocities.

codimension-two points poses some interesting questions for the nonlinear analysis which we shall address in the following sections.

In a comparison with experimental observations carried out with inhomogeneous systems, it is important to distinguish between convective and absolute instability as has been done, for example, by Lingwood (1997) in problems of flows over rotating disks. Since we are interested primarily in the nonlinear evolution of the secondary forms of flows we have confined ourselves to the normal mode analysis discussed in this section.

## 4. Secondary solutions and their stability for moderate rotation

The properties of the steady roll solutions evolving from the growing disturbances for $\Omega \lesssim 25$ can be described well by the numerical solutions based on the Galerkin representation (2.9). The finite-amplitude rolls reduce the stress on the boundaries as indicated in figure 6. The shear ratio $S$ has been plotted, which is defined as the shear exerted on the boundary divided by the shear corresponding to the basic solution (2.4),

$$S = \left| \frac{\partial \boldsymbol{U}_0}{\partial z}\bigg|_{z=1/2} + \sum_n n\pi \boldsymbol{d}_n \right| \Big/ \left| \frac{\partial \boldsymbol{U}_0}{\partial z}\bigg|_{z=1/2} \right|. \tag{4.1}$$

Obviously, the shear ratio is defined in analogy to the Nusselt number which measures the convection heat transport in a fluid layer heated from below. Since $\partial \hat{\boldsymbol{U}}/\partial z$ is proportional to the square of the amplitude of the fluctuating component of motion $S - 1$ provides a convenient measure for this amplitude. The direction of the shear is measured by the angle $\gamma$ according to the definition (2.5). As the amplitude of the secondary solution increases, $\gamma$ tends towards lower values indicating a tendency of the secondary solution to counteract the effects of rotation. Besides the definition (4.1) for the total shear ratio, the directional shear ratios $S_x, S_y$ parallel and perpendicular to the motion of the boundaries will be used in the following based on the expressions

$$S_x = 1 + \sum_n n\pi d_{nx} \Big/ \frac{\partial U_{0x}}{\partial z}\bigg|_{z=1/2}, \quad S_y = 1 + \sum_n n\pi d_{ny} \Big/ \frac{\partial U_{0y}}{\partial z}\bigg|_{z=1/2}. \tag{4.2}$$

The decrease of the shear at the boundaries may seem surprising since it can be easily proven that the shear stress can only be increased in the time-averaged sense in the case $\Omega = 0$ when the basic state of plane Couette flow is replaced by any other state of flow. But for $\Omega \neq 0$ a different situation occurs in that the onset of secondary states of flow can partially release the constraint of rotation. The energy balance is

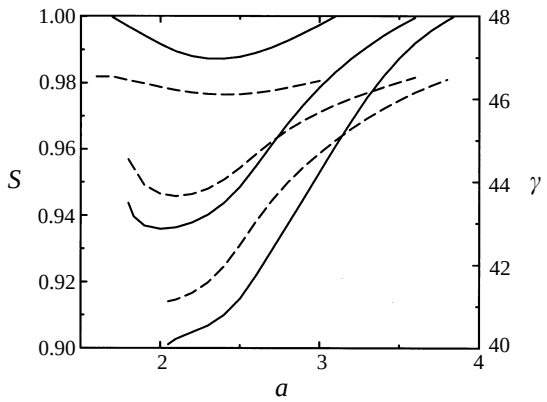


FIGURE 6. Shear ratio $S$ (solid lines) and direction of stress at the boundary given by the angle $\gamma$ (dashed lines) as a function of the wavenumber $a$ for $Re = 1000, 2000, 3000$ (from top to bottom) in the case $\Omega = 17$, $\varepsilon = 8°$.

given by

$$-Re\frac{\mathrm{d}}{\mathrm{d}z}U_x|_{z=1/2} = \left\langle \left| \frac{\mathrm{d}\boldsymbol{U}}{\mathrm{d}z} \right|^2 \right\rangle + \langle |\nabla\boldsymbol{\delta}\phi|^2 + |\nabla\boldsymbol{\varepsilon}\psi|^2 \rangle \tag{4.3}$$

where the angular brackets indicate the average over the fluid layer which is assumed to be time independent. The same assumption has been made for simplicity for the left-hand side. Although the addition of the fluctuating components $\boldsymbol{\delta}\phi$ and $\boldsymbol{\varepsilon}\psi$ of the velocity field increases the viscous dissipation on the left-hand side of (4.3), this increase may be more than compensated by a decrease of the viscous dissipation of the mean flow component. As a result the left-hand side can become smaller for the secondary state than for the basic state. The disturbance velocity field at finite amplitude does not differ much from the infinitesimal disturbance field shown in figure 3($a$) except that the region of negative streamfunction $\partial\phi/\partial\eta$ is enlarged in comparison with the region of positive $\partial\phi/\partial\eta$. This property reflects the reduction of the shear in the layer. The same effect is demonstrated more directly in figure 7($a$) where the mean flow profiles of the secondary state are compared with those of the basic state. When the total velocity field is plotted as in figure 7($b$) only cat's-eye-type vortices remain visible corresponding to minima of vorticity in the $\eta$-direction.

We have already mentioned in the preceding section that there are regions in the parameter space where the growth rate $\sigma$ of the steady mode of instability decreases with increasing Reynolds number and the basic state thus becomes stable again. In figure 8 such a finite region of instability is shown. The computations of finite-amplitude steady secondary solutions indicate that they exist only within this region. The dependence on $Re$ of the shear ratios $S_x$ and $S_y$ also given in that figure demonstrates this fact in the special case of the wavenumber $a = 3.1$. There is thus no indication of subcritical finite-amplitude instability.

By superimposing infinitesimal disturbances of the form (2.12) we can determine the region of stability of secondary solutions. As an example the stability region is shown as function of $Re, a$ and $\varepsilon$ in figure 9 for the case $\Omega = 17$. Most restrictive is the onset of the skewed varicose instability. This instability corresponds to infinitesimally small values of $b, d$ at the stability boundary. But beyond the boundary the values of $b, d$ maximizing $\sigma_r$ increase until $b$ reaches

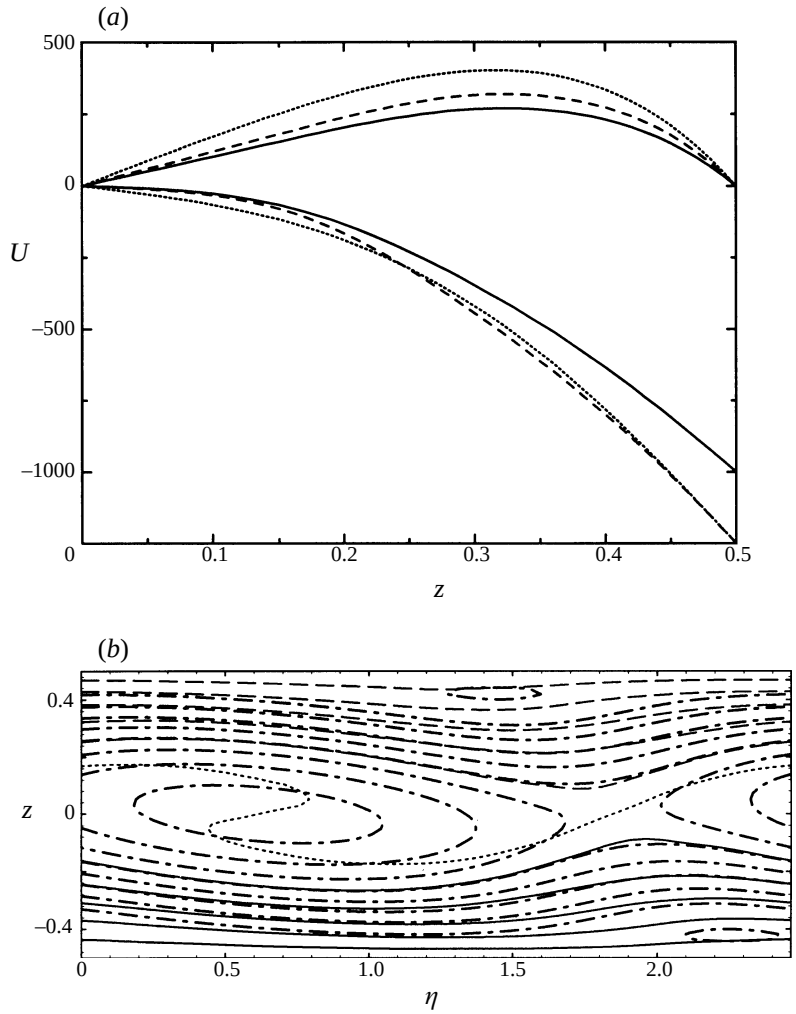


FIGURE 7. (*a*) Profiles of the mean flow $U_x$ (lower lines) and $U_y$ (upper lines) are shown for the secondary steady state in the case $\Omega = 17$, $a = 2.55$, $\varepsilon = 8.94°$ with $Re = 2000$ (solid lines) and with $Re = 2500$ (dashed lines). In the latter case the corresponding profiles for the basic state (2.4) (dotted lines) are shown for comparison. The continuation of the profiles into the region $z < 0$ of the layer is antisymmetric with respect to $z = 0$. (*b*) Streamlines (dash-dotted lines) in the $(\eta, z)$-plane and lines of constant velocity in the $\xi$-direction – solid (dashed) lines for positive (negative) values, the dotted lines indicate the zero value – in the case $\Omega = 17$, $Re = 2500$, $a = 2.55$, $\varepsilon = 8.82°$.

values of the order $a/2$. The maximum growth rate $\sigma_r$ is approximately reached for $d/b \approx 2$. Towards low wavenumbers the stability region is primarily restricted by the wavy instability which is characterized by vanishing $d$. The wavenumber $b$ is infinitesimal at the stability boundary and increases for the strongest growing wavy disturbance in proportion to the distance from the stability boundary. For large values of $\varepsilon$ the stability boundary moves towards higher values of $a$ until the region of stable secondary solutions disappears at an angle $\varepsilon$ of slightly above 11°. Also indicated in figure 9 are the sideband instability boundaries corresponding to the growth of the Eckhaus-type disturbances, i.e. disturbances with small $d$ and vanishing $b$.

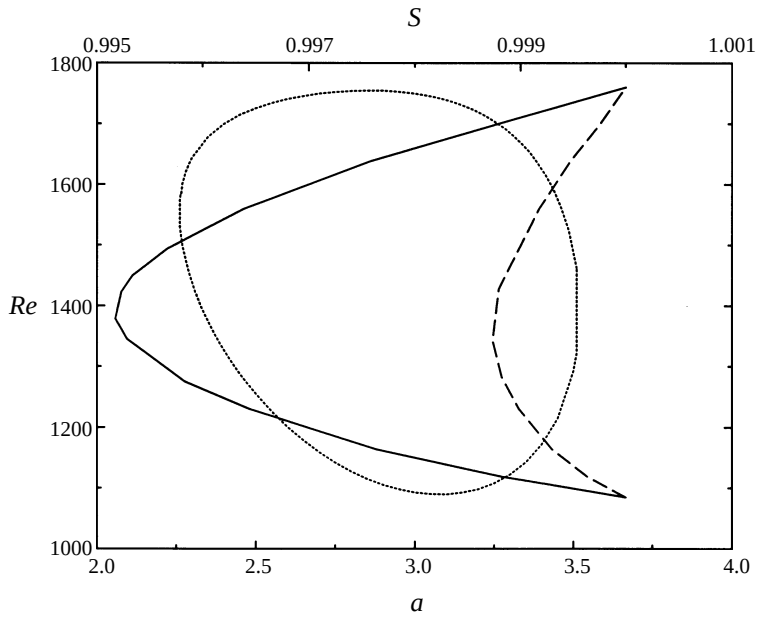


FIGURE 8. The neutral curve, $\sigma_r = 0$ (dotted line) for $\Omega = 17$, $\varepsilon = 16.5°$ and the shear ratios $S_x$ (dashed) and $S_y$ (thin solid line) in the case $a = 3.1$ corresponding to the scale on the upper abscissa.

It is often useful to study instabilities even when they are preceded by the onset of other instabilities. Since the latter may exhibit low growth rates they can be overtaken by the onset of instabilities at higher Reynolds number, but with stronger growth. The Ekman–Couette system offers typical examples of such a situation as shown in figure 10. In experiments with differentially rotating disks in which the Ekman–Couette layer is realized locally, the Reynolds number typically increases quite rapidly with respect to the system moving with the mean flow. It thus must be expected that short-wavelength instabilities with their high growth rates will be observed instead of the more weakly growing instabilities that set in at lower Reynolds numbers. In the particular case of the high-frequency instability with $\sigma_i \approx 840$ indicated by the thick solid line the wavenumber $b$ is only about 2.0. But its growth rate exceeds that of competing instabilities not far above onset. The extended stability diagram in figure 10 shows besides the onset of the high-frequency instability also the onset of an amplitude instability which is characterized by a finite value of $\sigma_i$, but does not break the symmetry of the steady rolls. The values of $\sigma_i$ are much lower than those for the high-frequency instability. But they vary considerably from the value 72 at $a = 2.0$ to the value 35 at $a = 2.8$. Because the real part of its growth rate does not increase much with $Re$ the amplitude instability cannot be expected to play a significant role in experiments. Of interest is the sharp bend of the right-hand branch of the Eckhaus instability boundary which abruptly turns towards lower values of $a$ with increasing $Re$. Because a crossing of stability boundaries corresponding to different eigenvalues $\sigma$ was suspected at first, this region of the parameter space was investigated in great detail. The bend is sharp, but of finite curvature. We have not been able, however, to identify a property of the steady roll solution associated with this bend.

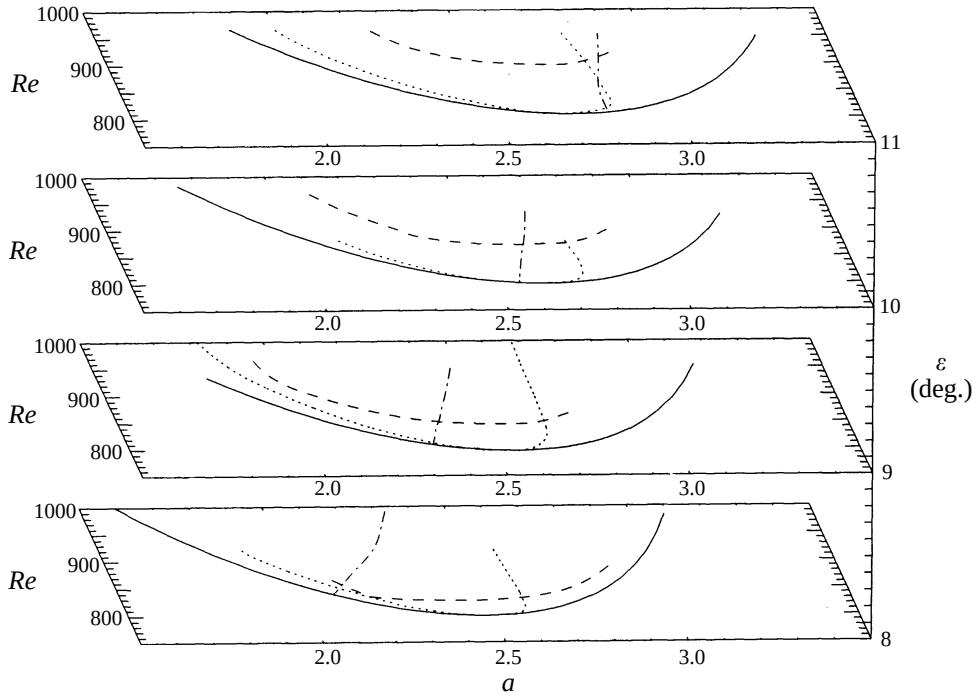


FIGURE 9. Regions of stability for steady roll solutions in ($Re$, $a$)-planes for different values of the angle $\varepsilon$ as indicated in the case $\Omega = 17$. The region of stability is the enclosed domain in each of the four panels. It is bounded by the onset of the skewed varicose instability (dashed lines) towards high values of $Re$ for $\varepsilon = 8°$, $9°$ and $10°$, by the wavy instability (dash-dotted lines) towards low values of $a$, and by the Eckhaus instability (dotted lines) towards high values of $a$ for $\varepsilon = 9°$, $10°$ and $11°$ (and also towards low values for $\varepsilon = 8°$).

## 5. Secondary solutions in the case of strong rotation

At high rotation rates corresponding to $\Omega$-values of the order 100 the Ekman instability of type II sets in first according to results of figure 4($a$). This instability leads to waves propagating towards the right of the shear in the respective boundary layers. The type II wave can be described by the representation (2.9) when the coordinate $\eta$ is replaced by $\eta - ct$ where $c$ is the phase velocity of the wave. The Newton–Raphson iteration can be applied in the same way as in the case of the steady solution except that we must fix the phase of the wave by setting the imaginary part of one of the coefficients, say $a_{11}$, equal to zero. The corresponding equation is then available for the determination of $c$. As in the case of the steady secondary solution at lower values of $\Omega$ the type II wave leads to a decrease of the shear exerted at the boundary. But the shear ratio $S$ decreases less rapidly with increasing $Re$ than in the case of the steady roll solution. For example $S$ reaches a maximum of 0.985 at about $a = 2.8$ for $Re = 1000$ and a minimum of 0.979 at $a = 2.4$ for $Re = 1500$. The corresponding angles $\gamma$ are 43.5° and 42.6°, respectively, and the angle $\varepsilon$ is 22.7° in both cases. The fluctuating component of the flow field of the mode propagating along the lower boundary does not change much from that shown in figure 3($b$) as $Re$ increases. A slight asymmetry develops between positive and negative parts of the streamfunction. But the nature of this asymmetry changes with varying parameters and does not seem to have much physical significance.

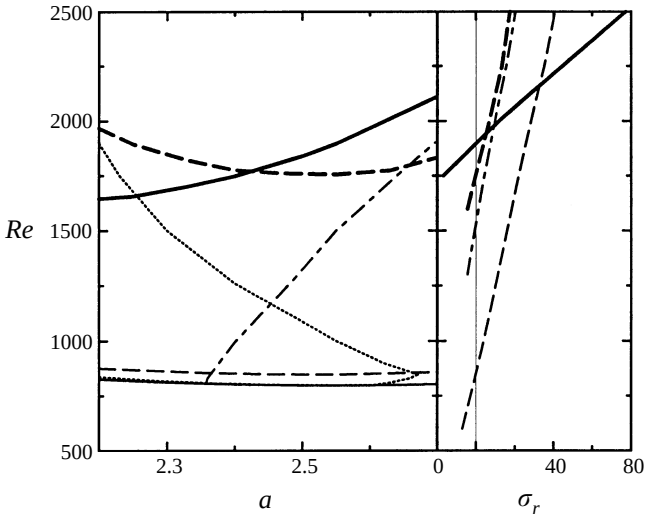


FIGURE 10. Onset of instabilities as a function of the wavenumber $a$ of steady rolls is shown on the left-hand side in the case $\Omega = 17$, $\varepsilon = 8.94°$. The thin dashed, the long dash-short dash and the dotted lines indicate the onset of the skewed varicose, the wavy and the Eckhaus instabilities, respectively, as in figure 9. The thick line indicates the onset of the high-frequency instability and the thick dashed line refers to the onset of amplitude oscillations. Growth rates $\sigma_r$ of the instabilities are shown on the right-hand side of the figure in the particular case $a = 2.55$.

The stability of the type II wave solution can be analysed in terms of the general disturbances of the form (2.12) as in the case of steady secondary solutions after the coordinate $\eta$ has again been replaced by $\eta - ct$. A special problem arises in that there are two wave solutions propagating in opposite directions along their respective Ekman boundary layers. In the physical situation both waves are realized. But since their interaction is rather minimal and decreases to zero with increasing $\Omega$, it is justified to consider the stability of a single wave. The instability corresponding to the growth of the wave at the opposite boundary will be ignored for this reason. The other instabilities studied here are also confined to the boundary along which the type II wave travels. It thus can be expected that they will be little influenced by a second wave travelling along the opposite boundary. The results of the stability analysis in the special case $\Omega = 100$ are plotted in figure 11. There are three different instabilities characterized by values of $b$ of the order $a/2$ which have been named for simplicity $\alpha$-, $\beta$-, $\gamma$-instabilities. They differ in their typical frequencies. But the size of the frequency corresponds roughly to that expected on the basis of the advection by the mean flow at the distance from the boundary where the maximum amplitude of the mode is located. A vanishing Floquet wavenumber $d$ was found in all cases. In addition there is a high-wavenumber instability which sets in at a much higher Reynolds number than the other ones, but it is of physical importance because of its much more strongly increasing growth rate $\sigma_r$. The value of $b$ is of the order $3a$ and the frequency $\sigma_i$ is of the order 4000 at the stability boundary. In contrast to the $\alpha$- and $\beta$-instabilities its amplitude is very much confined to the region near the boundaries. The $\gamma$-instability also exhibits a strong confinement to the boundary region, but not as strong as that of the high-wavenumber instability.

The high-wavenumber instability appears to correspond quite well to the secondary instability found in the numerical simulation of Marlatt & Biringen (1995) of the

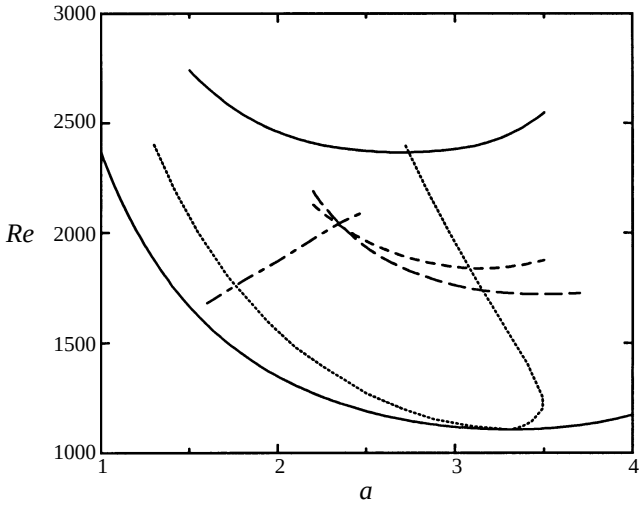


FIGURE 11. Stability region of type II waves in the $(R, a)$-plane in the case $\Omega = 100$, $\varepsilon = 20.45°$. The region of stable waves is bounded by the onset of the Eckhaus instability (dotted line) from below and the onset of the $\alpha$-instability (long dash-short dash line) and the $\beta$-instability (long dash line) from above. Also shown are the onset of the $\gamma$-instability (short dash line) and the high-wavenumber instability (solid line).

evolution at finite amplitudes of the type II Ekman layer instability. None of the instabilities found in the Reynolds number range of figure 11 can be interpreted as a modifed type I instability and we must conclude – as have Marlatt & Biringen – that the onset of the type II instability stabilizes the layer to the onset of type I instabilities.

A detailed analysis of finite-amplitude properties of type I waves has not been done in the present context since this instability is usually preceded by the onset of type II waves. But the formulation of the Ekman–Couette problem offers the attractive feature of a codimension-two point where the onset of type I and type II waves coincide. In the neighbourhood of this codimension-two point a weakly nonlinear analysis leads to coupled amplitude equations for the two competing modes. After separating the complex amplitudes for the type I and type II waves into their absolute values $A$ and $B$, respectively, and their phases we obtain equations of the form

$$M_I \dot{A} = (Re - Re_I)A - (\gamma_{IA}A^2 + \gamma_{IB}B^2)A, \tag{5.1a}$$

$$M_{II} \dot{B} = (Re - Re_{II})B - (\gamma_{IIA}A^2 + \gamma_{IIB}B^2)B, \tag{5.1b}$$

with constant real coefficients $M_i, \gamma_{ik}$, with $i = I, II$ and $k = A, B$. Since there seem to be no possibilities for resonances and since the waves interact only through the mean flow components, the phases of the waves do not enter equations (5.1). The evaluation of the coefficients gives rise to the bifurcation diagrams shown in figure 12. The diagrams indicate that mixed solutions, $A \neq 0, B \neq 0$, are stable only in a small region of the parameter space and that type I waves appear to be the preferred mode in the competition between the two instabilities near the codimension-two point. It should be noted that in writing equations (5.1) we have assumed that no connection exists to the analogous combination of waves at the opposite boundary. Because of the rather weak interaction between the waves propagating in opposite directions

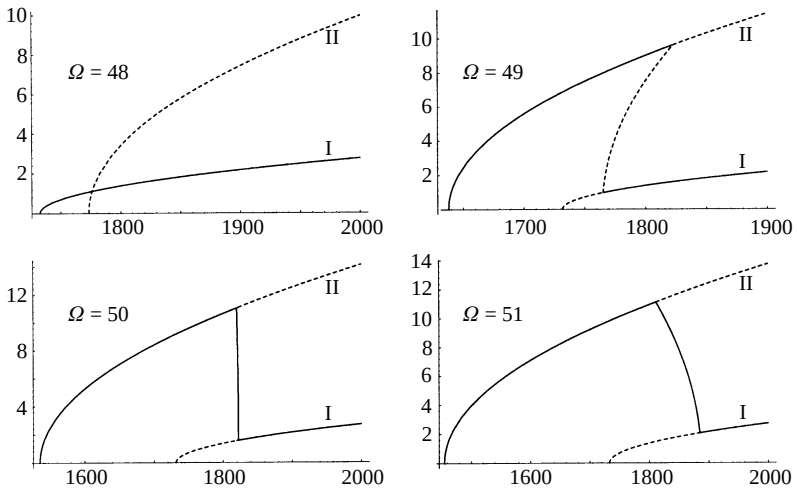


FIGURE 12. Bifurcation diagrams for several values of $\Omega$ close to the codimension-two point of type I and type II Ekman layer instabilities. Plotted are the amplitudes $A, B$ as functions of the Reynolds number $Re$.

along the two boundaries it appears to be justified to restrict attention to the type I and type II waves at one of the boundaries.

## 6. Tertiary states of fluid flow

It is evident from the preceding sections that the regions in the parameter space where two-dimensional secondary solutions are stable are rather restricted. Here we intend to follow the evolution of some of the typical secondary instabilities. In principle the Galerkin method can be employed for this purpose through the use of expansion functions of the form $\exp\{\mathrm{i}la_\xi\xi + \mathrm{i}ma_\eta\eta\}$ with time-dependent coefficients $a_{lmn}(t)$ etc. In practice a spectral collocation method with Chebyshev polynomials as expansion functions for the $z$-dependence was used. Because the nonlinear terms are evaluated in real space the method is computationally more efficient for time integrations than a purely spectral method based on the Galerkin representation. For details we refer to the books by Canuto *et al.* (1988) and Fletcher (1991).

We first describe tertiary solutions in the low rotation case. The skewed varicose instability exhibits wavenumbers $b$ and $d$ which grow with distance from the stability boundary and saturate at about $d = 0.85$ and $b = 0.4$ for $a = 2.55$. We have thus chosen $a_\xi = b$ and $a_\eta = a/3$ in order to accommodate the evolving skewed varicose pattern within the periodicity interval in the $(\xi, \eta)$-plane. An example of a steady skewed varicose pattern is shown in figure 13. This flow appears to be less efficient in reducing the shear stress at the boundaries than the roll solution as is apparent from figure 14 where shear ratios of the two solutions are compared. As the Reynolds number is increased, the skewed varicose pattern becomes replaced by rolls with a larger wavelength. This feature appears to be the result of the Eckhaus instability which not only occurs for two-dimensional rolls with $a = 2.55$ according to figure 9, but also affects the three-dimensional skewed varicose pattern. In the computations based on the $\xi, \eta$-periodicity interval used for figure 14 the return to two-dimensional solutions manifests itself in the form of an approximate superposition of roll solutions with two and with three wavelengths in the $\eta$-interval. The shear ratios are still closer

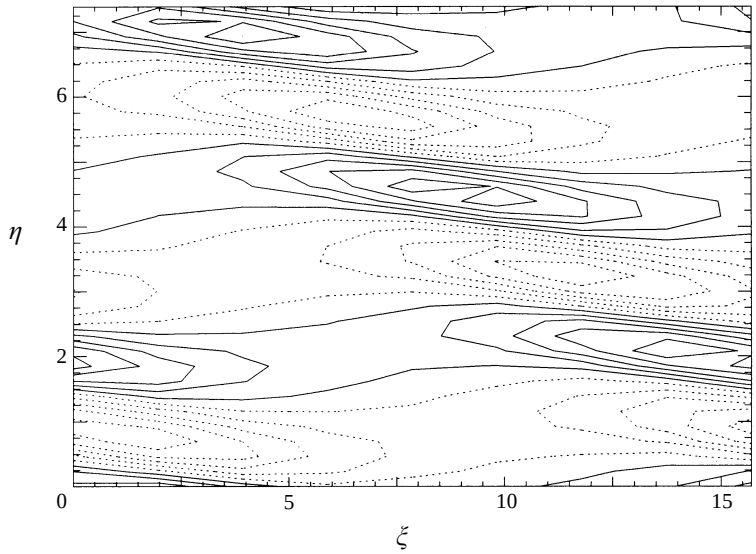


FIGURE 13. Lines of constant $z$-component of the velocity field in the plane $z = 0$ for finite-amplitude skewed varicose rolls in the case $\Omega = 17$, $Re = 980$, $\varepsilon = 8°$, $a = 2.55$.

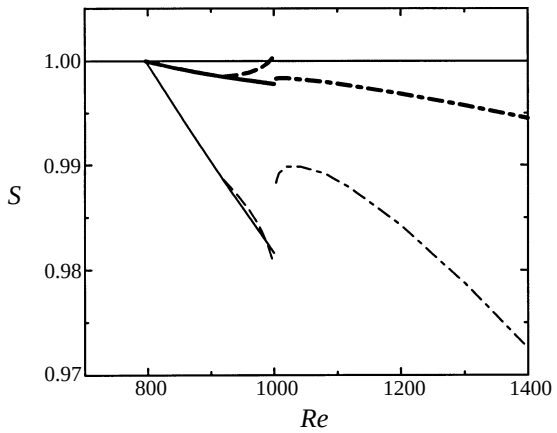


FIGURE 14. Shear ratios $S_\xi$ (thick lines) and $S_\eta$ (thin lines) for rolls (solid lines) and skewed varicose rolls (dashed lines) bifurcating from them in the case $\Omega = 17$, $\varepsilon = 8°$, $a = 2.55$. The definition of $S_\xi$ and $S_\eta$ is analogous to that of $S_x$ and $S_y$ given by expression (4.2). For the computation of the skewed varicose rolls the same periodicity interval as in figure 15 has been used. For $Re \geqslant 1000$ a two-dimensional solution is found again corresponding to a superposition of rolls with $a = 2.55$ and with $a = 2 \times 2.55/3$.

to unity than for the original roll solution since the momentum transport decreases with $a$ in the relevant range of wavenumbers $a$.

The wavy instability is another instability of importance in the stability diagrams of figures 9 and 10. It does not seem to lead to a new pattern, but instead replaces the given rolls with those of a smaller angle $\varepsilon$ and a corresponding higher value of $a$.

Of particular interest is the evolution of the high-frequency mode which in contrast to the other tertiary solutions is more confined to the boundary layers. There are actually two modes of this kind which travel in opposite directions near the respective

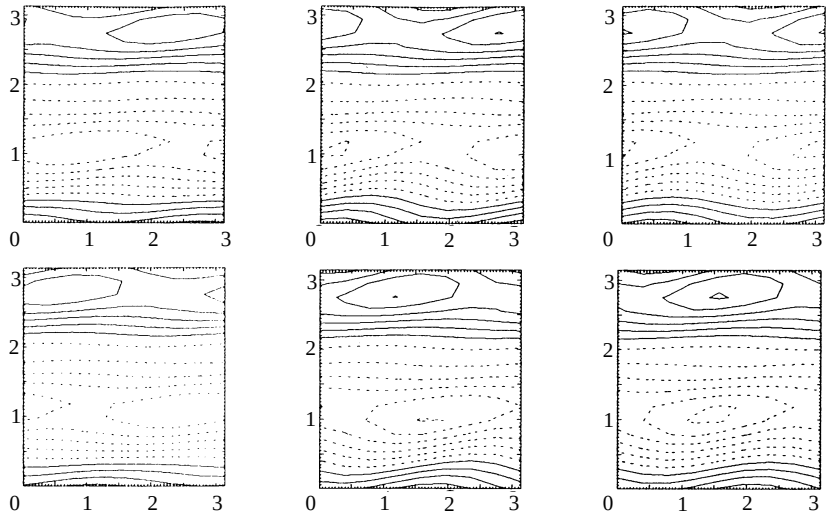


FIGURE 15. Lines of constant $z$-component of the velocity field in the plane $z = 0$ in the case $\Omega = 17$, $Re = 1700$, $\varepsilon = 8°$, $a_\eta = 2.0$, $a_\xi = 2.0$. The time sequence of plots (upper row left to right, then lower row) shows the onset of the high-frequency instability travelling in opposite $\xi$-directions in the respective boundary layers. Accordingly three-dimensional features travel in the positive (negative) $\xi$-direction where the $z$-velocity is positive (negative). The seventh plot would be nearly identical to the first plot.

boundaries. The numerical simulations visualized in figure 15 show that both modes are excited with equal amplitude resulting in an oscillatory flow in which structures travel in the positive (negative) $\xi$-direction in regions of positive (negative) $z$-velocity. The shear ratio does not show any noticeable time dependence and remains essentially unchanged from the value in the case of rolls.

In the case of the onset of instabilities of the type II Ekman waves it is more difficult to follow the evolution of the disturbances to higher amplitudes. The combination of the $\beta$- and $\gamma$-instabilities leads to slightly deformed varicose rolls which remain steady with respect to an appropriately moving coordinate system. They are more efficient in reducing the stress on the boundaries than the type II Ekman waves as has been found in all examples for which computations have been done. The $\alpha$-instability does not seem to lead to a three-dimensional pattern, but instead reorientates the type II waves and thereby shifts them into the stable domain.

## 7. Some further results

Not all bifurcations indicated by the stability boundaries in §§4 and 5 have yet been discussed. The amplitude instability which affects the two-dimensional state with high wavenumbers as indicated in figure 9 can be investigated rather easily through forward integrations in time since the tertiary state of flow remains two-dimensional. The shear ratio $S$ exhibits increasing amplitude of oscillation with slightly decreasing period as the Reynolds number increases. When $Re$ exceeds 2200 a period-doubling cascade is realized and chaotic solutions are found beyond $Re \approx 2400$. But at these high Reynolds numbers the state of flow has probably long been unstable with respect to three-dimensional disturbances which have not been investigated.

Besides the long-wavelength instability of the type II Ekman waves mentioned in the preceding section there is also the high-wavenumber instability indicated in

the stability diagram of figure 11. The time integrations that have been undertaken in order to follow the evolution of this instability have not yielded purely periodic states. Instead the shear ratio exhibits aperiodic bursts. This feature matches the explosive behaviour of the secondary instability which prevented Marlatt & Biringen (1995) reaching an amplitude saturated state in their simulation. Rather similar high-frequency short-wavelength disturbances have been observed experimentally (Lerche 1996) as instabilities of stationary cross-flow vortices in the related problem of the three-dimensional boundary layer over a swept wing. Further time-consuming numerical integrations will be needed to study the mechanism of these bursts and their dependence on parameters of the problem. We thus postpone a more detailed discussion to a later publication.

Another topic we briefly wish to mention is isolated solitary roll solutions that occur for values of $Re$ below the onset of secondary states of flow. These solitary rolls solutions do not bifurcate from any other known solution branch. Preliminary results are included in a recent PhD thesis (Hoffmann 1997), but their detailed description and the analysis of their stability properties will require additional work.

## 8. Concluding discussion

The results described in this paper show a rich variety of dynamical processes as a function of the external parameters $Re$ and $\Omega$ of the system. Although the basic state is more complex than the more familiar basic parallel flows in non-rotating fluid channels such as Poiseuille flow and plane Couette flow, the Ekman–Couette system offers the advantage that the symmetry-breaking bifurcations induced by instabilities can be physically realized because they usually occur in a supercritical fashion. The presence of rotation obviously provides access to degrees of freedom which are not accessible in the case of plane Couette flow, for instance, since this flow does not exibit a bifurcation from the basic state.

The regular patterns observable on rotating disks in fluids have long attracted the attention of experimenters. The theoretical model treated in this paper can at best be applied locally for typical experimental configurations. Nevertheless we cannot resist the temptation of a comparison of the results of §§ 4 and 5 for the onset of secondary motions with the recent experimental observations of Schouweiler *et al.* (1996). These authors used a rotating disk enclosed in a cylindrical box with the same inner radius $R$. By varying the height $h$ of the fluid above the disk they could vary the ratio between the dimensionless rotation rate and the shear. Since the rigid cylindrical wall of the experiment introduces a strong inhibiting influence on the Ekman shear flow of the system and since the observations of flow structures were typically made at a distance of $0.7R$ to $0.8R$ from the axis we use the conditions at the distance of $0.7R$ for the definition of the parameters $\Omega$ and $Re$. The theoretical predictions of the onsets of the three instabilities agree quite well with the experimental observations as shown in figure 16. Besides the inhomogeneous conditions in the experiment the fact that the instabilities must reach a finite amplitude to become observable must be taken into account in assessing the quantitative agreement between theory and experimental results.

Transitions to tertiary states of flow are also often observed in experiments, usually in the form of high-wavenumber structures along the roll-like patterns of the secondary states of flow. The comparison between theory and observations is much more difficult to achieve in this case and we have not yet attempted to relate computed wavelengths and frequencies of tertiary states to experimental measurements.

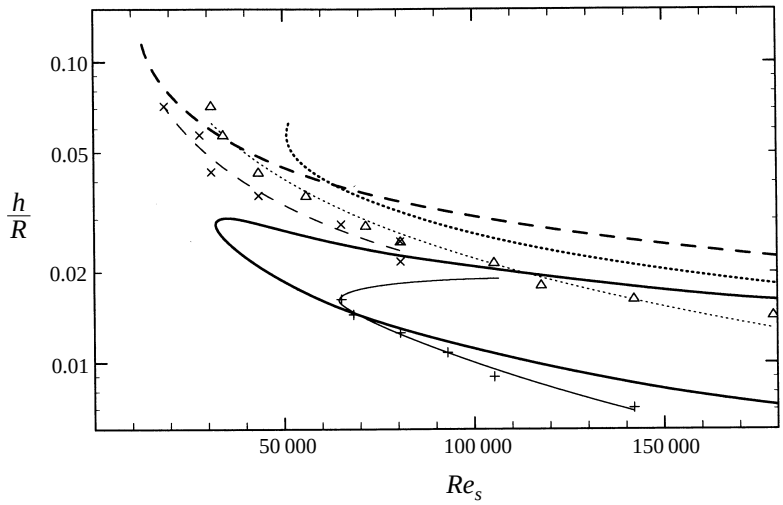


FIGURE 16. The results of Schouweiler *et al.* (1996) (thin lines connecting symbols for experimental observations) in comparison with the predictions of figure 4(*a*) (thick lines). The solid (+), dotted (△) and dashed (×) lines indicate the onset of steady rolls (with respect to the theoretical frame of reference), type I and type II Ekman waves, respectively. The Reynolds number $Re_S$ based on the radius $R$ of the rotating disk as length scale and the height $h$ are used in the figure.

Preliminary earlier work on the subject of this paper by Chen (1981) has been supported by the Atmospheric Sciences Section of the US National Science Foundation.

## REFERENCES

CANUTO, C., HUSSAINI, M. Y., QUATERONI, A. & ZANG, T. A. 1988 *Spectral Methods in Fluid Dynamics.* Springer.

CHANDRASEKHAR, S. 1961 *Hydrodynamic and Hydromagnetic Stability.* Clarendon.

CHEN, W.-L. 1981 Shear flow instabilities in a rotating system. Dissertation, University of California at Los Angeles.

CLEVER, R. M. & BUSSE, F. H. 1997 Tertiary and quaternary solutions for plane Couette flow. *J. Fluid Mech.* **344**, 137–153.

FALLER, A. J. 1962 An experimental study of the instability of the laminar Ekman boundary layer. *J. Fluid Mech.* **15**, 560–576.

FALLER, A. J. & KAYLOR, R. E. 1966 A numerical study of the instability of the laminar Ekman boundary layer. *J. Atmos. Sci.* **23**, 466–480.

FLETCHER, C. A. J. 1991 *Computational Techniques for Fluid Dynamics.* Springer.

HOFFMANN, N. P. 1997 Beiträge zur Theorie der Ekman-Schicht. Dissertation, University of Bayreuth.

JARRE, S., LEGAL, P. & CHAUVE, M. P. 1996 Experimental study of rotating disk instability. I. Natural flow. *Phys. Fluids* **8**, 496–508.

LERCHE, T. 1996 Experimental investigation of nonlinear wave interactions and secondary instability in three-dimensional boundary-layer flow. In *Advances in Turbulence VI* (ed. S. Gavrilakis, L. Machiels & P. A. Monkewitz), pp. 357–360. Kluwer.

LILLY, D. K. 1966 On the instability of Ekman boundary flows. *J. Atmos. Sci.* **23**, 481–494.

LINGWOOD, R. J. 1997 Absolute instability of the Ekman layer and related rotating flows. *J. Fluid Mech.* **331**, 405–428.

MARLATT, S. W. & BIRINGEN, S. 1995 Numerical simulation of spatially evolving Ekman layer instability. *Phys. Fluids* **7**, 449–451.

PRESS, W. H., FLANNERY, B. P., TEUKOLSKY, S. A. & VETTERLING, W. T. 1986 *Numerical Recipes.* Cambridge University Press.

SCHOUWEILER, L., LEGAL, P., CHAUVE, M. P. & TAKEDA, Y. 1996 Experimental study of the stability

of the flow between a rotating and a stationary disk. In *Advances in Turbulence VI* (ed. S. Gavrilakis, L. Machiels & P. A. Monkewitz), pp. 385–388. Kluwer.

Tatro, P. R. & Mollo-Christensen, E. L. 1967 Experiments on Ekman layer instability. *J. Fluid Mech.* **28**, 531–543.

Zandbergen, P. J. & Dijkstra, D. 1987 Van Kármán swirling flows. *Ann. Rev. Fluid Mech.* **19**, 465–491.